MuPET (Multiphysics PET): Bridging Computational Mass Transport Physics and Medical Imaging for Synthetic Positron Emission Tomography Data Generation

Sai Kiran Kumar Nalla[1, *], Quentin Maronnier[2], John A. Kennedy[3,4], Sebastian Uppapalli[5], Olivier Caselles[2,6]

1. IUTC - Institut universitaire du cancer de Toulouse, Universite de Toulouse, Toulouse, France
2. Department of Medical Physics, Oncopole Claudius Regaud, IUTC Oncopole, Toulouse, France
3. Department of Nuclear Medicine, Rambam Health Care Campus, P.O.B. 9602, 3109601 Haifa, Israel
4. Ruth and Bruce Rappaport Faculty of Medicine, Technion Israel Institute of Technology, Haifa, Israel
5. Department of Aerospace and Mechanical Engineering, École Centrale School of Engineering, Mahindra University, Hyderabad, India – 500043
6. Tachyons SAS, Toulouse, France

***Correspondence & Statistical Analysis:**

Sai Kiran Kumar Nalla

PhD Student, Year 3, Université de Toulouse

IUTC - Institut universitaire du cancer de Toulouse, 1 Av. Irène Joliot-Curie, 31100 Toulouse

Email: sai-kiran-kumar.nalla@utoulouse.fr

Quentin Maronnier: **The work for this manuscript was conducted while affiliated with Oncopole Claudius Regaud, Toulouse, France**

Word Count: 6305 (4219 – Introduction, Methods, Results, Discussion, Abbreviations, Disclosures)

Abstract:

Purpose: Robust positron emission tomography (PET) research increasingly requires reliable ground-truth activity distributions, yet clinical data and physical phantoms cannot provide them fully. This work introduces MuPET (multiphysics PET), a computational framework that bridges mass-transport physics simulation with image domain noise modeling to generate realistic, synthetic PET images.

Methods: Tracer transport and radioactive decay within a custom phantom geometry were modeled via decay diffusion physics. The simulated activity concentrations were converted into PET equivalent count maps, followed by a pseudo-Poisson noise model calibrated to scanner-specific characteristics. MuPET generated images were compared with experimental PET acquisitions and a conventional synthetic lesion insertion pipeline. VOI (volume of interest) and ROI (region interest) data extraction was performed on all the data. The quantitative metrics included the recovery coefficient (RC), target contrast ratio (TCR), coefficient of variability (COV), and activity profile.

Results: The simulated effective activities matched the decay-corrected measurements within 0.4–1.2%, confirming high physics-model fidelity. The optimized noise model achieved COV values (3.9–4.0%) comparable to those of the acquisitions (3.8–3.9%). MuPET demonstrated strong agreement with the experimental profiles and quantitative metrics, with mean biases within 10% of the acquisition.

Conclusion: MuPET establishes a fast (approximately 15 min), physically grounded pipeline that combines transport modeling with PET image simulation, enabling generation of realistic datasets. This approach provides a practical foundation for future dynamic PET simulations.

Graphical Abstract:

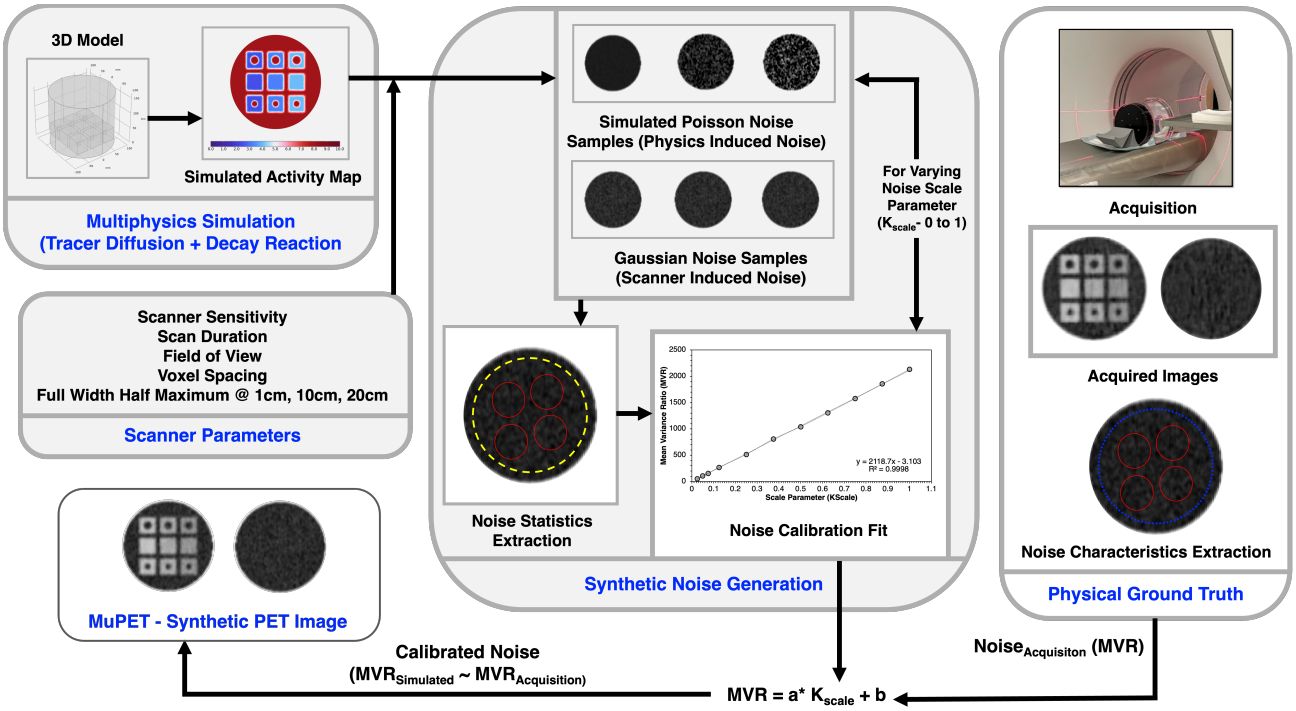

Introduction:

Positron emission tomography (PET) in combination with computed tomography (CT) imaging offers unique insights for the early diagnosis of cancer [1–3]. Robust quantitative PET analysis, radiomics pipelines, and data-driven imaging methods increasingly require reliable ground-truth activity distributions to benchmark performance [4–6]. However, clinical PET acquisitions alone cannot provide true ground truth data due to biological variability and ethical limitations. Traditionally, simpler systems such as standardized phantoms are designed for benchmarking quantitation and image quality tests across generations of scanners to generate ground truths [7]. However, current phantoms lack the customizability necessary to mimic anatomically realistic conditions accurately [8–10].

To address this need, PET simulation frameworks have been developed, ranging from analytical models to highly detailed Monte Carlo tools such as SimSET or GATE [11,12]. These simulators replicate detector physics and photon transport with high fidelity. However, their computational expense and complexity make them impractical for rapid iteration and large-scale dataset generation. Projection-domain lesion-insertion methods such as DUETTO [13,14], PETSTEP (PET simulator of tracers via emission projection) [15], SMART PET (SiMulAtion and ReconsTruction) [16] and FAST PET (fast analytical simulator of tracers) [17] offer faster alternatives. They inserted synthetic activity directly into sinograms prior to vendor reconstruction. While these approaches can approximate clinical acquisition pipelines, they rely on a baseline PET scan or ideal activity source map with additional noise modeling. Models often combine Poisson, pseudo-Poisson, or gamma-based assumptions for replicating stochastic noise [18–22]. However, these approaches remain constrained by the availability of baseline PET scans and offer limited flexibility for creating synthetic data in new geometries or dynamic conditions.

In parallel, three-dimensional (3D) printing has emerged as a key experimental tool for creating more realistic customizable anthropomorphic phantoms at a lower cost [23–27]. This facilitates the rapid prototyping of complex models, allowing for the inclusion of tissue heterogeneity and detailed lesion morphologies. The adaptability of 3D-printed phantoms across facilities for standardization and harmonization studies has also been established [10,28,29]. However, this alone cannot meet the demands of scalable ground-truth generation, since every new design iteration must still be physically manufactured, filled, and imaged. Thus, the limitation underscores the broader need for computational models to create synthetic PET data for ground truths. With the advent of digital twins various medical domains have long relied on physics-based modeling, including cardiovascular modeling [30,31], perfusion simulation [32], and drug delivery modeling [33]. Despite widespread research, very little work has extended such transport-based modeling approaches to medical imaging, especially PET. Few studies have incorporated diffusion modeling to generate time activity curves and activity distribution maps but not synthetic images [34–37]. Mass transport-based solvers naturally support time-dependent dynamics, making them uniquely suited for dynamic imaging [34]. Additionally, the potential for patient-specific PET simulations could be explored to fill gaps in simulators for theranostic and dynamic imaging applications.

In this work, we introduce MuPET (multiphysics PET), a framework that combines diffusion–reaction modeling with a pseudo-Poisson PET noise model to generate realistic PET-like images from arbitrary geometries. We aim to validate the framework against experimental PET data and conventional lesion insertion data to demonstrate strong quantitative agreement alongside improved adaptability and computational efficiency.

2. Methods:

2.1 Experimental Phantom Acquisition and Synthetic lesion Insertion

A custom imaging phantom (**Fig. 1**.**a**) adapted from [26], was used as the physical reference system for evaluating the MuPET framework. It consists of a Jaszczak cylindrical container fitted with nine 3D-printed permeable cubes (40 mm) of acrylonitrile butadiene styrene (ABS). The cubes were designed with permeable walls to allow uniform filling and were assigned three controlled dilution levels (50%, 60%, and 70%) relative to the background solution. Six cubes contained internal spherical cavities (15 and 20 mm diameter) to emulate the lesions, whereas the remaining three were solid reference units to emulate the tissue (**Fig. 1**.**b**). The phantom was prefilled with a water/soap solution 4–5 hours prior to image acquisition. Fifteen minutes prior to the scan, 56.7 MBq of ^{18}F-FDG radiotracer was injected into the estimated 6.2 L volume. This ensured a well-defined initial condition for both the physical measurements and the computational model. All acquisitions (**Fig. 1**.**c**) were performed using a single bed position on a Discovery MI PET/CT platform (*GE Healthcare, Chicago, IL, USA*) across three consecutive frames of 300 seconds each with a single CTAC (CT attenuation correction). The activity at the time of the scan was decay-corrected relative to the injected activity. PET data were reconstructed into a 384 × 384 × 89 volume with a voxel spacing of [1.042, 1.042, 2.8 mm] via Q.Clear FX BPL (*Bayesian penalized likelihood reconstruction with a regularization parameter, TOF*, β: 550). The detailed phantom preparation protocol and acquisition parameters can are followed as per guidelines by a previous study [29].

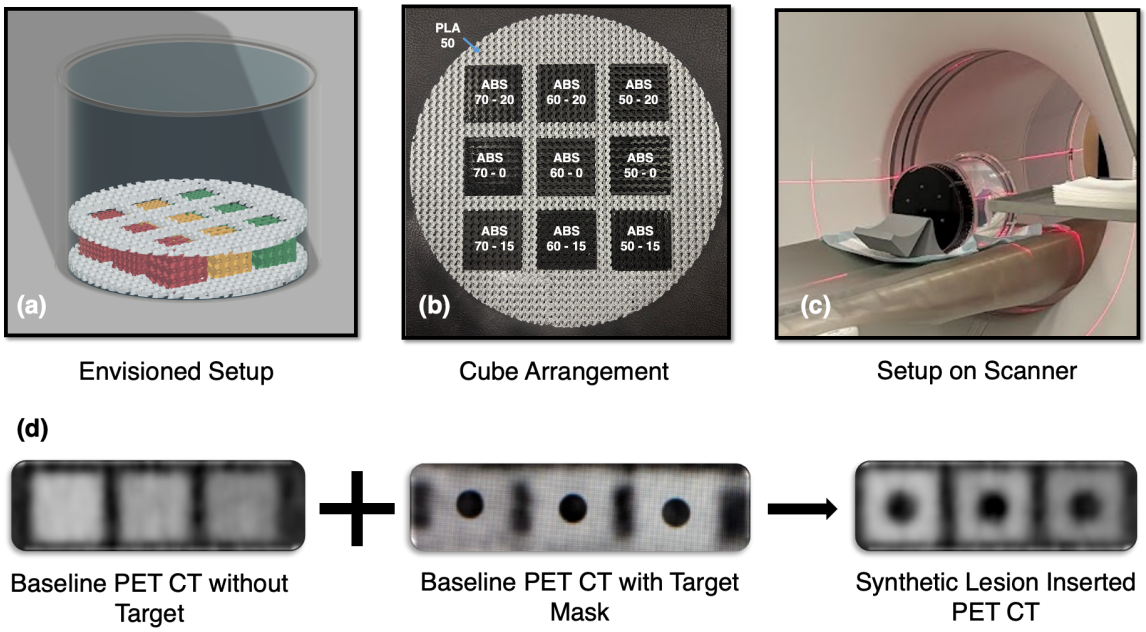

Fig. 1 (a) 3D rendering of the adapted phantom design; (b) Arrangement of cubes – (Notation: percentage of ABS – target size); (c) Bed leveling on a PET/CT scanner; (d) Summarized workflow of synthetic lesion insertion

Synthetic lesion insertion was subsequently performed on the basis of a workflow proposed by [14] via the Duetto Toolbox (*GE Healthcare, Chicago, IL, USA*). This step was included to provide a benchmark against a conventional lesion-insertion workflow to enable a direct comparison with MuPET's physically modeled synthetic data. Spherical binary masks of 15 and 20 mm were created and positioned on the reference cubes (no target) in the acquired PET images (**Fig. 1d**). Inserted synthetic lesions (ISLs) were created by specifying the target-to-background activity ratio with respect to the reference cube measurements to the generated masks, which were converted into simulated sinograms. This was added to the raw sinogram, and the final lesion-inserted images were generated through a reconstruction process and parameters matching the acquisitions.

2.2 MuPET Framework:

The MuPET (multiphysics PET) framework introduced here presents a computationally efficient pipeline for simulating PET image data. This approach combines COMSOL Multiphysics® (*COMSOL*

Inc., Stockholm) based tracer distribution modeling with a synthetic noise modeling postprocessing workflow.

2.2.1 Numerical Modeling:

Conservative mass transport was modeled via a diffusion-reaction formulation (**Eq. 1**), assuming concentration-driven passive movement coupled with first-order radioactive decay. The simulation geometry for the numerical simulation was constructed based on experimental dimensions and measurements adjusted to measure the fillable volume, as represented in **Fig. 2a.**

$$\frac{\partial C_i}{\partial t} = \nabla.(D.\nabla C_i) - (\lambda * C_i)\ ;\ \lambda = \frac{\log 2}{T_{1/2}} \qquad (1)$$

where C_i is the concentration in mol/m^3, D is the diffusion coefficient (m^2/s), λ is the decay factor (1/s), and $T_{1/2}$ is the half-life (s).

The activity concentration (AC) in kBq/mL was converted to C_i in mol/m^3 based on **Eq. 2**. A no-flux boundary condition was applied to the outer walls (**Eq. 3**). The initial activity concentration in the background (AC_{in}) for the simulation was derived as the injected activity divided by the injection volume. Initial background concentrations AC_{in} were derived from the injected activity/volume and modulated to establish target contrast levels (i.e., 0.5 × AC_{in}, 0.4 × AC_{in}, or 0.3 × AC_{in}, respectively).

$$C_i = \frac{AC_i}{(\lambda * N_A)}\ ;\ N_A = 6.02 \text{ x } 10^{23} \qquad (2)$$

where N_A is Avogadro's number in mol^{-1} and AC is the activity concentration in kBq/mL.

$$-n.(D.\ \nabla C_i) = 0 \qquad (3)$$

All material properties within the numerical model were assumed to be analogous to those of ^{18}F-FDG and water, and in instances where specific properties were not readily available, corresponding values for glucose were adopted as a reasonable approximation. The properties used are as follows: density of the fluid (ρ): 1.00 g/mL; diffusion coefficient of FDG in water (D): 6 × 10^{-10} m^2/s is adapted from the value of glucose [38]; half-life of tracer ($T_{1/2}$): 110 minutes [36]. To validate the modeled

geometry, volume-averaged activity (MBq) in the domains was compared with decay-corrected values from acquired image DICOM metadata. The computational domains were discretized and independence of the concentrations sampled at 726 (11 × 11 × 6) different locations, with an acceptable threshold of 5% across 3 grid sizes for numerical stability was verified. The simulations were computed for 35 minutes with a step size of 1 min via an iterative solver.

2.2.2 Synthetic noise modeling

Noise modeling was performed entirely in the image domain to account for PET physics noise and scanner resolution effects and few reconstruction-induced effects.

(a) The simulated activity maps $AC_{Simulated}$ (x, y, z, t) in kBq/mL were exported as a 4D volume with spatial dimensions matching the experimental scan volumes of 383 × 383 × 89 (1.042 × 1.042 × 2.8 mm^3). Additionally, the maximum and minimum values of activity concentration within the computational domain are exported as functions of time $AC_{Max}(t)$ and $AC_{Min}(t)$.

(b) Upon import into MATLAB (*MathWorks INC, MA, USA*), postprocessing, including data cleaning and reorientation to the FOV, was performed if necessary. The volumes are also separated into individual 3D volumes.

(c) 3D activity maps were converted to expected counts (CTSs) via **Eq. (4**), which includes T_{scan} (scan duration), $S_{scanner}$ (scanner sensitivity), and V_{voxel} (voxel volume) adapted from NEMA (National Electrical Manufacturers Association) [39]

$$\mathrm{CTS}(x, y, z) = \mathrm{AC}_{\mathrm{simulated}}(x, y, z) * \mathrm{S}_{\mathrm{scanner}} * \mathrm{T}_{\mathrm{scan}} * \mathrm{V}_{\mathrm{voxel}} \qquad (4)$$

(d) The resulting count volume $\mathrm{CTS}\ (x, y, z)$ was then subjected to a pseudo Poisson model: the counts were multiplied by an adjustable scale factor to generate $\mathrm{CTS}_{\mathrm{scale}}(x, y, z)$, after which Poisson noise was generated to introduce PET physics-based noise $\mathrm{CTS}_{\mathrm{N}}(x, y, z)$. Then, the noisy data were normalized back with a scale factor $\mathrm{C}_{\mathrm{NP}}(x, y, z)$ to maintain the mean variance ratio (MVR) as K_{scale} [20].

$$CTS_{scale}(x,y,z) = K_{Scale} * \ CTS(x,y,z) \qquad (5)$$

$$\lambda(x,y,z) = \max\left(0, CTS_{scale}(x,y,z)\right) \qquad (6)$$

$$CTS_N(x,y,z) \sim Poisson\left(\lambda(x,y,z)\right); \quad P(CTS_{scale}(x,y,z) = a) = \frac{e^{-\lambda_{x,y,z}} * \lambda_{x,y,z}}{a!} \qquad (7)$$

$$C_{NP}(x,y,z) = \frac{CTS_N(x,y,z)}{K_{scale}} \qquad (8)$$

$$E[C_{NP}] = \frac{\lambda_{x,y,z}}{K_{scale}} \ \& \ Var(C_{NP}) = \frac{\lambda_{x,y,z}}{(K_{scale})^2} \qquad (9)$$

$$MVR_{Effective} = K_{scale} \qquad (10)$$

(e) To simulate inherent resolution limitations, the AC_{map} was convolved with a spatially variant, anisotropic Gaussian kernel. The full width at half maximum (FWHM) of the kernel was derived from scanner specifications as per AAPM (American Association of Physicists in Medicine) Task Group 126 (TG-126) findings [40]. A detailed mathematical description and the values of the FWHM used for the Gaussian model are included in the supplementary information.

To create a scanner and acquisition-dependent dataset of the simulated noise, iterative variations of K_{scale} from 1 down to 0 were performed. For each value, a noisy volume was generated. The mean variance ratio (MVR) for each generated sample was computed via two distinct methods: 2D region of interest (ROI) extraction across six randomly chosen uniform slices and 3D volume of interest (VOI) extraction for a 75 mm uniform activity section from the center to the top of the phantom. On the basis of the extracted noise characteristics, the best fit between the calculated MVR values and their corresponding K_{Scale} values was performed.

2.3 Data extraction and statistical tests:

The PET volume was categorized into 3 different regions: reference water, background cubes and targets for data extraction. Quantitative data extraction was carried out via the VOI (matching

physical dimensions of the target) approach following the workflow of [14,26] on Image Interpretation Software - Volume Viewer, PETVCAR® (*GE Healthcare, Chicago, IL, USA*) for experimental and ISL data, MATALB for MuPET. The activity values in kBq/mL were extracted semiautomatically. Additional ROIs (30 mm for cubes, 20 mm for reference water) and central activity profile extractions were performed for distribution analysis. For the ROI, a total of 13 circular ROIs—9 (ϕ 30–9 cubes) and 4 (ϕ 20–4 background water)—were placed automatically on the central cross-sectional slice with the targets. Two quantitative metrics were calculated from the extracted VOI data, namely, the recovery coefficient (RC), which was used to quantify the recovered true activity concentrations, and the target contrast ratio (TCR), which was used to assess the contrast of lesions against the background (Eqs. 9 & 10).

$$\mathrm{RC}_{(\mathrm{mean/max})} = \frac{\text{Activity concentration in VOI (Mean/Max)}}{\text{Theoretical activity concentration}} \qquad (9)$$

$$\mathrm{TCR}_{(\mathrm{mean/max})} = \frac{\text{Activity Concentration in target volume (Mean/Max)}}{\text{Activity Concentration in corresponding reference cube (Mean)}} \qquad (10)$$

$$\text{Coefficient of Variability (CV)} = \frac{\text{Standard Deviation } (\sigma)}{\text{Mean } (\mu)} \text{ x } 100 \qquad (11)$$

The coefficient of variability for the uniform regions was also calculated via Eq. (11) based on the extracted VOI data of acquisition and MuPET. Detailed statistical tests for the 3 quantitative metrics were not performed because of the lower target sample size of N_{Sample} = 6 for each set, and the standard percentage error and Bland–Altman bias with limits of agreement were calculated. All the extracted activity data were initially checked for normality via the Shapiro–Wilk test. This was followed by a two-sided Brown test and *equal* variance test on the ROI data of acquisition (Acq), and MuPET was chosen because of its reduced dependence on normality. Finally, the activity profiles for MuPET vs Acq and MuPET vs ISL were followed up by Wilcoxon rank sum test (also known as the

Mann–Whitney test) for the assessment of central tendency-driven significant differences. All tests were performed with a significance of $p < 0.05$ in JASP (*JASP Team, Netherlands*).

3. Results:

3.1. Phantom Acquisition and Synthetic Lesion Insertion:

The observed Hounsfield units (HUs) of the CT values of the reference cubes were 4.6 ± 4.8 (TBR ~ 2), 4.5 ± 3.5 (TBR ~ 2.5), and 7.6 ± 4.3 (TBR ~ 3.33), which fell within the range of water (3.1 ± 3.7) (**Fig 2.a, 2.b**). All the different regions were captured effectively via PET acquisition (PET Acq), with different contrasts being visibly distinguishable (**Fig 2.c, 2.d)**. Additionally, the inserted synthetic lesions (ISLs) represented the actual targets well enough, and a visual comparison based on the target diameter was performed (**Fig 2.c, 2.d).**

3.2. Mass Diffusion and Decay Reaction Simulation:

The computational phantom, as depicted in **Fig. 3.a**, was estimated as a 6.23 L volume. The effective activity (MBq) calculated from the volume-averaged simulated activity concentration was compared against the analytically decay-corrected experimental values (DICOM metadata) (**Fig. 3.b**). The percentage differences observed for the activity were low, ranging only from 0.43% to 1.16%, confirming high model fidelity. Numerical stability was validated through a grid convergence study **(Fig. 3.c).** Effective convergence was achieved between 0.6 and 1 million tetrahedral elements, and a final mesh of 1 million tetrahedral elements was selected for all subsequent analyses. This specific configuration resulted in a computational time of ~ 10 minutes for a total simulated decay of 35 minutes (with a time step of 1 minute). The central cross-sections of the activity concentrations for the 3 corresponding time steps are shown in **Fig.** 3d, with observed maximum–minimum values of 8.26–2.16, 8.10–2.13, and 7.84–2.09 kBq/mL (averaged across 3 frames).

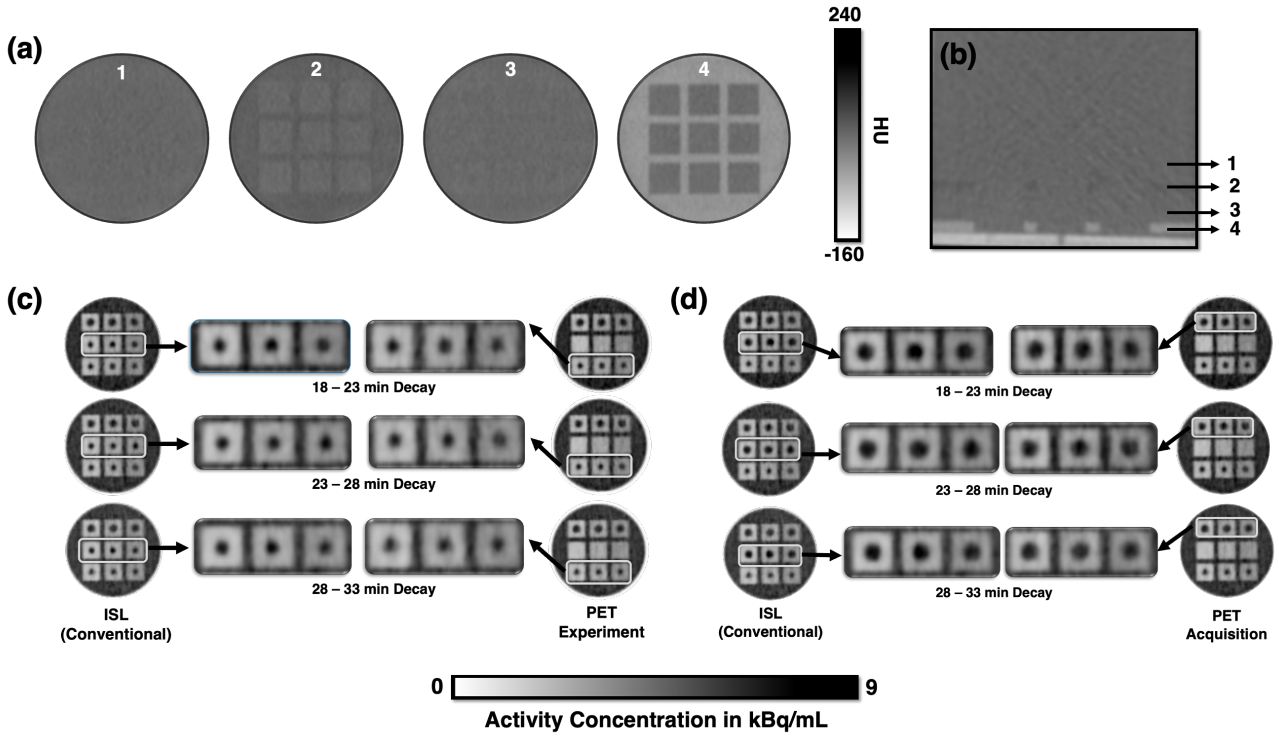

Fig. 2 (a) Cross-sectional CT AC slices at 4 different locations (1. Pure water, 2. ABS cubes with ABS support, 3. Cubes with water; 4. ABS cubes with PLA support) **(b)** Corresponding location of CT slices; Central PET slice with exploded target view of ISL vs. PET acquisition for 3 frames **(c)** 15 mm, **(d)** 20 mm

3.3. Noise characterization and MuPET modeling:

For the PET noise model, the $MVR_{acquisition}$, which was determined from scan data on the basis of a central VOI measuring Φ 18 cm × 7.5 cm, yielded MVR = 85.8. Additionally, MVR values extracted from ten random uniform slices utilizing an 18 cm ROI [19] resulted in a consistent range of values between 75 and 95. The pseudo-Poisson noise model for simulation was calibrated by varying the scale factor K_{scale} between 0.005 and 1. **Fig. 4a,b** shows samples of the simulated noise, illustrating how this parameter influences the noise distribution. This process established a linear relationship between the resulting MVR_{Noise} and K_{scale} (**Fig. 4.a**). Notably, this fit is intrinsically specific to the scanner properties and Gaussian used in the scanner model. Using the linear fit, a global K_{scale} of

0.0415 was selected, yielding a resultant MVR_{sim} = 85 thus calibrated to acquisition value. This optimized noise model resulted in coefficient of variation (CV) values for MuPET (3.9-4.04%) that closely matched the acquired PET data (3.75-3.91%).

3.4. Quantitative comparison of PET profiles and metrics:

The extracted ROI data distributions were compared via kernel density estimation (KDE) (**Fig. 5**). The activity profiles extracted along the central vertical axis are presented in **Fig. 6a.** The target profiles exhibited a Gaussian-like peak, characteristic of partial volume effects (PVEs), confirming the integrated resolution blurring effect. In addition to visual assessment, quantitative metrics provide deeper insight into the model's performance. The recovery coefficients and target contrast ratios averaged over 3 frames are presented in **Fig. 6.b, 6.c & 6.d**. Bland–Altman bias analysis was used to quantify the differences between methodologies (**Table 1**). Compared with acquired PET, MuPET tended to slightly underestimate the maximum values (RC_{Max}, TCR_{Max}), whereas the ISL method generally overestimated these metrics. All the mean values were within a comparable range of bias of 10% of acq.

Table. 1 Bland–Altman mean bias percentage with limits of acceptance (mean ± 1.96 * SD) for quantitative metrics

Quantitative Metric	Acq vs ISL	Acq vs MuPET	ISL vs MuPET
RC_{Max}	-9.84 ± 4.02	9.64 ± 6.98	10.27 ± 4.04
RC_{Mean}	0.33 ± 7.29	2.66 ± 9.72	2.32 ± 9.99
TCR_{Max}	-9.73 ± 4.29	2.34 ± 5.37	12.06 ± 2.94

The Brown-Forsythe test indicated no statistical evidence of variance (**Table 2**) for most conditions, except for the 50% reference cube and the uniform slice.

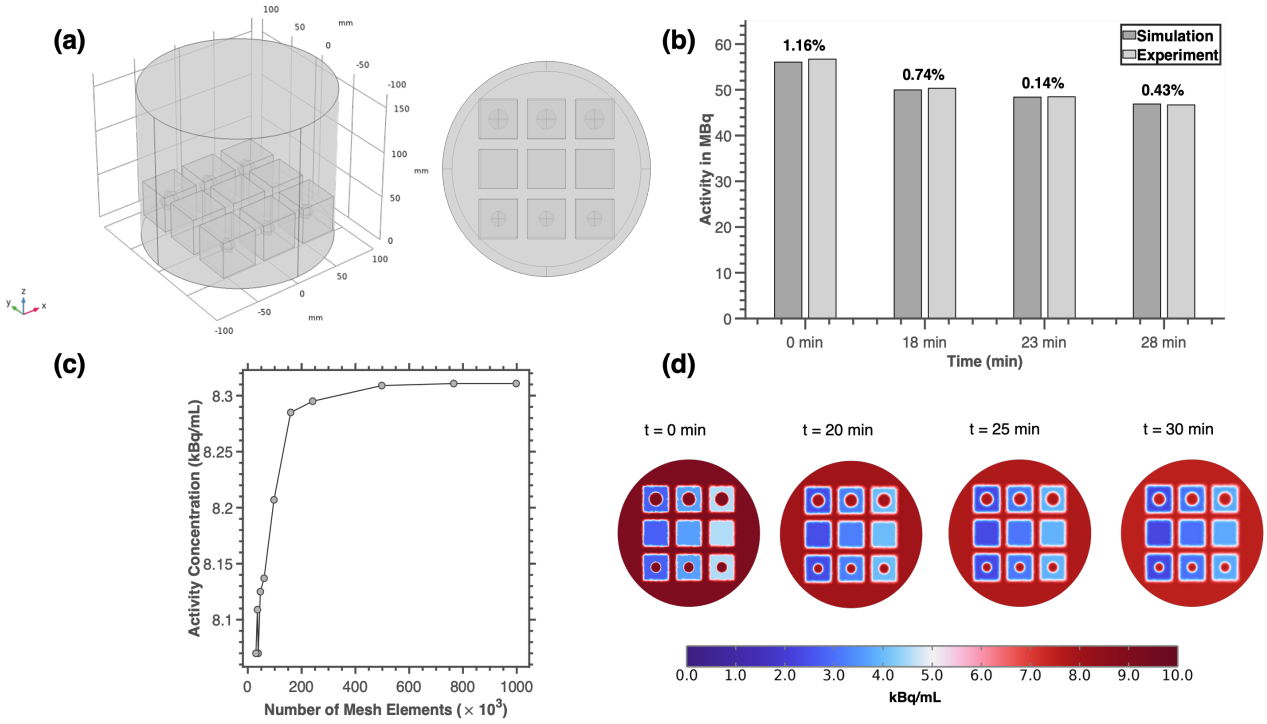

Fig. 3 (a) 3D rendering of the computational domain and axial (top view) geometric setup displaying targets and cubes following the experimental layout. **(b)** Comparison of the effective activity (in MBq) of the simulation with analytically calculated decay-corrected activity from DICOM metadata. **(c)** Grid convergence for the simulation. **(d)** Central cross-sectional slice for the simulated activity distribution at different time stamps prior to noise addition.

4. Discussion:

The MuPET framework, as introduced in this work, successfully integrates diffusion-reaction modeling with an empirical noise model and resolution blurring to generate realistic synthetic PET data. In this work, we validated our method exclusively via controlled phantom experiments. This choice was intentional, as phantoms provide a fully controllable and well-defined ground truth against which the underlying physics model and noise pipeline can be rigorously assessed. Model fidelity despite several approximations is validated by strong quantitative agreement between the simulated effective activity and the decay-corrected experimental values, with a variability of < 5%.

Our mass diffusion model effectively represents the tracer distribution. This is crucially validated by the qualitative and quantitative agreement between the simulated effective activity (**Fig. 3.b**) and the noise-free target activity profiles (**Fig. 3.d**), which follow experimental patterns.

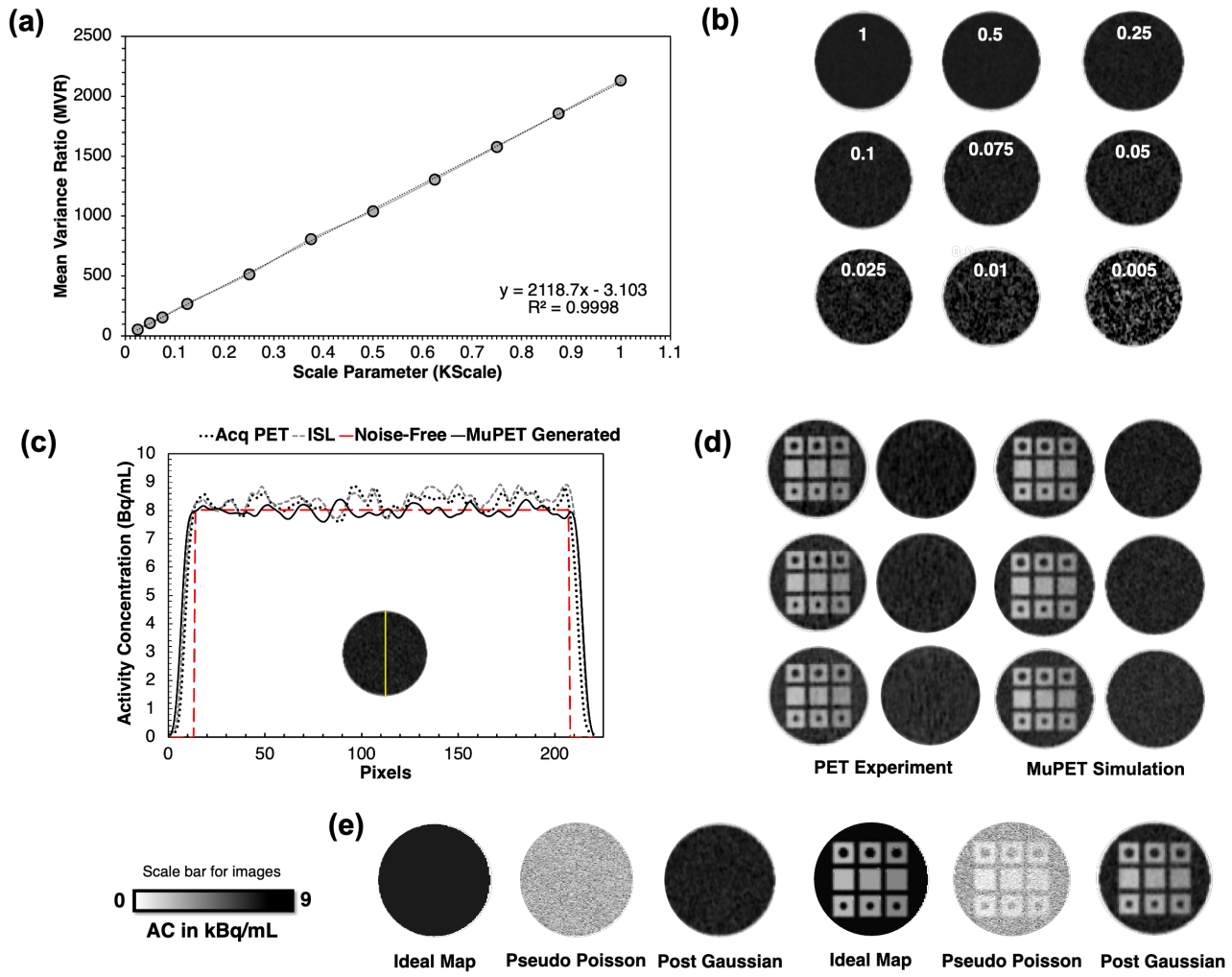

Fig. 4 (a) Linear fit for K_{Scale} as a function of MVR for the simulation map. **(b)** Cross-sectional slice of generated noise for different $_{KSc.}$ **(c)** Activity profile extracted experimental data, simulated map and corresponding generated noise for frame 1. **(d)** Background and target images of the 3 frames - Acquisition PET (COV_{BKG} – 3.75, 3.83, 3.91%) vs MuPET simulation for K_{Scale} ~ 0.03 (COV_{BKG} – 3.63, 3.64, 3.75%). **(e)** Overview of noise generation workflow for background and target slices.

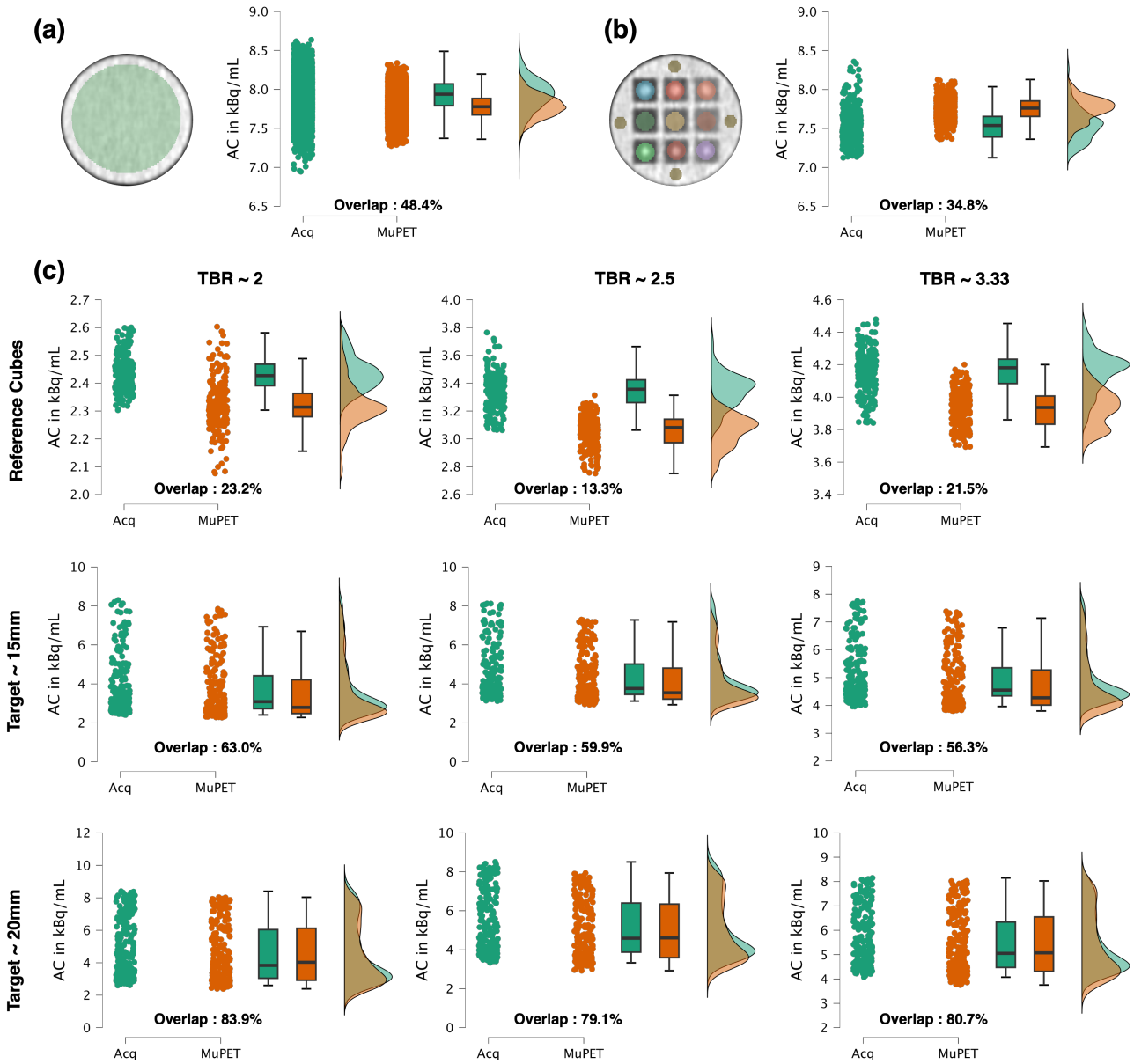

Fig. 5 (a) Extracted activity distribution for the 18 cm ROI on the uniform slice for MuPET vs Acq; **(b)** ROI placement (30 mm for cubes, 20 mm for water) and corresponding data distribution comparison for water ROIs; **(c)** Corresponding comparison of raincloud data distribution plots for cubes - reference cubes, 15- and 20-mm targets (rows); TCR ~ 2.00, 2.50, 3.33 (columns).

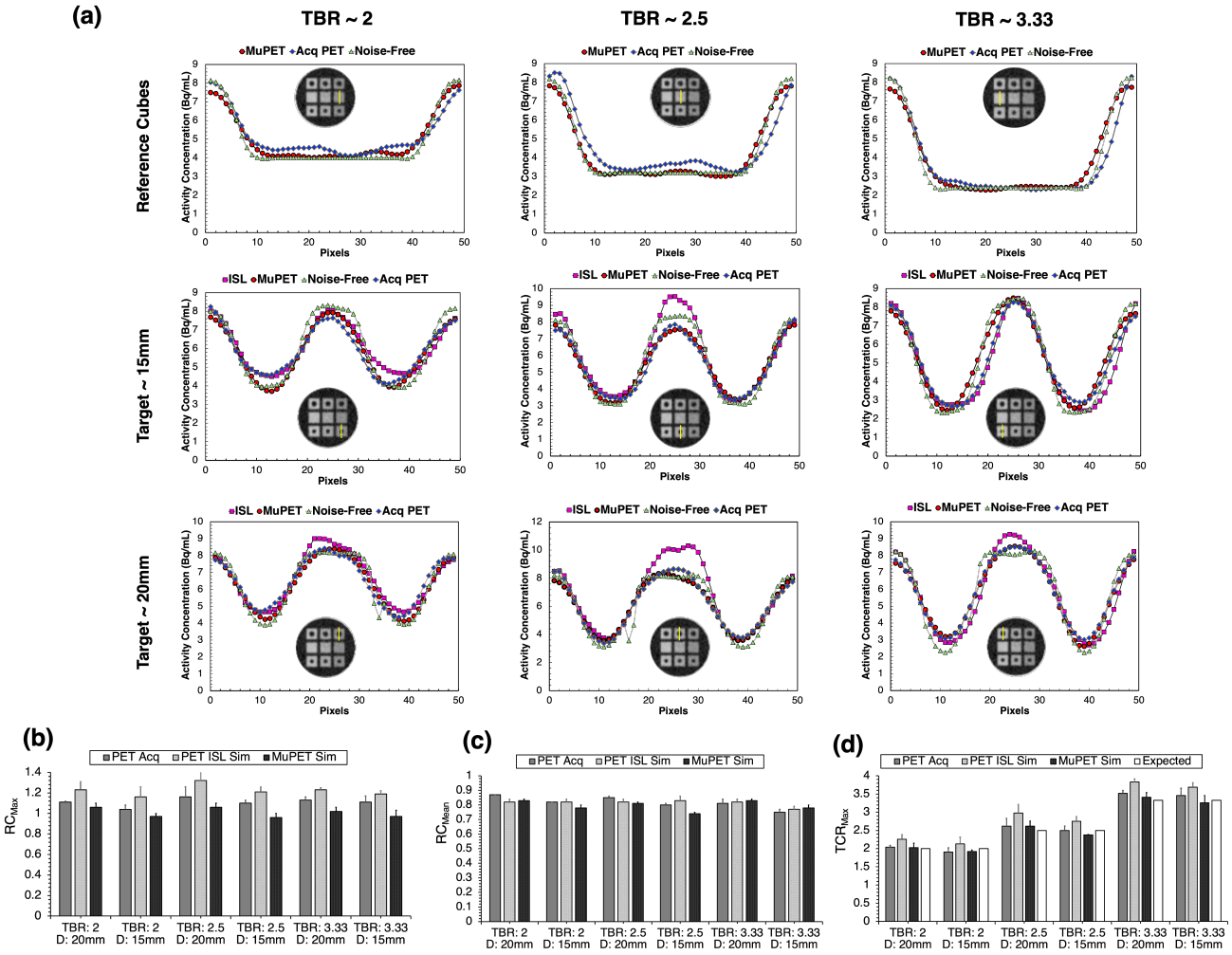

Fig. 6 (a) Vertical activity profile of cubes on a central cross-sectional slice – reference cubes and 15- and 20-mm targets (rows); TCRs ~ 2.00, 2.50, and 3.33 (columns). Averaged quantitative metric comparison based on VOI data for **(b)** RC_{Mean}, **(c)** RC_{Max}, and **(d)** TCR_{Max} (the corresponding data can be found in the supplementary information).

A key computational simplification is the assumption of bulk concentrations instead of modeling microlevel tracer uptake. This approximation is validated because the phantom's microlevel structural variations (pores typically < 4 mm) are smaller than the scanner's resolution. Consequently, the PET image captures only the average macroscopic tracer behavior, allowing the model to focus on bulk simulation while reducing the computational intensity by avoiding high refinement zones.

Table. 2 Summary of descriptive data & nonparametric statistical tests

		TCR ~ 3.33:1			TCR ~ 2.50:1			TCR ~ 2.00:1			Background
		R	15 mm	20 mm	R	15 mm	20 mm	R	15 mm	20 mm	
ROI Data	*Mean in kBq/mL (Coefficient of Variability %)*										
	Acq	2.44 (3%)	3.79 (40%)	4.62 (39%)	3.35 (4%)	4.42 (30%)	5.17 (29%)	4.16 (3%)	4.98 (19%)	5.49 (22%)	7.92 (3%)
	MuPET	2.32 (4%)	3.58 (42%)	4.56 (39%)	3.06 (4%)	4.13 (30%)	4.98 (31%)	3.93 (3%)	4.74 (21%)	5.44 (24%)	7.78 (2%)
	Brown Forsythe P – value: N_{Sample} ~ 17000 (For background), 990 (For rest)										
	-	0.01	0.75	0.85	0.45	0.69	0.63	0.63	0.49	0.08	0.001
Wilcoxon Rank Sum P – value: N_{Sample} ~ 442 (For background), 98 (For rest)											
Activity Profile (MuPET vs Acq)		0.91	0.79	0.80	0.001	0.97	0.72	0.008	0.69	0.54	0.05
Activity Profile (ISL vs Acq)		-	0.45	0.99	-	0.23	0.19	-	0.28	0.27	0.00135

We assume that the diffusion properties of the ABS cubes are identical to those of water + FDG. This choice is radiologically justified by the HU values [29] observed for the reference cubes in the CT acquisition (Section 3.1), which fall within the range of water. However, the true diffusivity in the cubes is much lower than that in the bulk water because of microscale geometrical variations. Although not observed in this study, the use of water properties in simulations risks overestimating diffusion over extended periods. In future, longer diffusion study is needed to assess scattering fully. A robust solution in this regard could be is to build an empirical dataset following homogenization principles: microscopic changes in permeability and diffusivity are mapped to a macroscopic value as a function of porosity. With respect to the pseudo scaled Poisson noise model, the primary goal was to mimic quantitative stochastic noise rather than voxel-based textural changes. In this regard, the models global MVRsim 85 resulted in CoV_{sim} values (3.9-4.04%) closely matching the acquired PET values (3.75-3.91%). However, some discrepancies can also be observed in the ROI data (**Table 2 & Fig. 5**). Across all evaluated target sizes, MuPET showed strong alignment with both acquisition and ISL for TCR_{max} and RC_{mean}. This is also supported by the close activity profiles (**Fig. 6.b**) to those of the

experiment and ISL. The resulting p values also indicate the absence of statistical evidence, although with some outliers. To assess partial volume effects (PVEs) accurately, a detailed analysis using common segmentation criteria, rather than 2D profiles, would be ideal for future work.

Notably, the conventional synthetic lesion insertion method consistently overestimates the values, especially RC_{max} and TCR_{max}. This is because applying the contrast ratio to a base experimental scan, which inherently carries PET noise multiplies the bias. In contrast, the results of the MuPET noise model were slightly underestimated compared with those of the experiment (**Table 2**), which can be attributed to two main factors: the simulation being instantaneous while experimental scans are acquired over time and the global application of the noise scaling parameter (K_{scale}) despite noise naturally increasing as activity concentration decreases. The former can be addressed by selecting the last timestamp or an average across time stamps corresponding to the scan duration instead of an intermediate time point. The latter requires that further iterations incorporate the dependence of K_{scale} on voxel intensity. Additionally, while we followed the noise characterization approach of [19], the MVR can be sensitive to the chosen ROI or VOI; a more robust analysis, such as noise power spectrum (NPS) analysis [17] or automatic slice-by-slice noise mapping [41], could better determine the noise characteristics. Another interesting phenomenon observed was that the overlap between the extracted ROI activity values was the worst for the reference cubes, and the target cubes provided the best representation. This accurate depiction of lesions is particularly promising considering that our noise model was generated based on uniform, nontarget slices. The higher COV for the target cubes (**Table 2**) is because the ROI (30 mm) includes the target and certain regions of background to obtain consistent measurements across methods for comparison. In this framework, the mean values are generally affected by the simulation, and the variance is affected by the noise model. The underestimation observed in low-activity reference cubes is due to the lack of voxel

intensity-based effects, i.e., the BPL algorithm used for acquisitions actively suppresses noise in these regions, which is not captured by the simple noise model. Hence, further noise model datasets are needed for various reconstruction settings.

In this work, the core objective was to introduce a fast, scalable computational pipeline centered on modeling tracer distributions. The MuPET pipeline achieves this with a total computation time of less than 15 minutes (activity map simulation to PET data generation) without a baseline PET scan while the ISL took around 12h with a baseline-scan. MuPET is not intended to be a replacement for high-fidelity clinical simulators or lesion insertion methods that can model the entire scan process but rather a new pragmatic approach for quick ground truth datasets. An interesting addition for future works would be a pipeline with an approximated CT attenuation map built from 3D models [42]. This enables the potential to include more reconstruction algorithms, thus reducing empirically derived relationships and opening avenues for comprehensive image quality studies. The adaptability of analogous MuPET frameworks for other imaging modalities can also be explored. The core strength lies in leveraging mass transport solvers like those used in cardiovascular modeling, which naturally support time-dependent dynamics. This opens the possibility to extend future works into complex, patient-specific simulations and dynamic imaging ground truths with better noise models.

Conclusion:

The MuPET framework successfully integrates multiphysics transport modeling with image-domain noise simulation to produce realistic synthetic PET data. Validated against physical phantom experiments, the method accurately predicts tracer distributions with high fidelity while replicating clinical noise characteristics. By utilizing mass transport solvers, MuPET establishes a practical foundation for future extensions into dynamic PET Image simulation.

References:

1. Engbersen MP, Van Driel W, Lambregts D, Lahaye M. The role of CT, PET-CT, and MRI in ovarian cancer. Br J Radiol. 2021;94:20210117. https://doi.org/10.1259/bjr.20210117

2. Hadebe B, Harry L, Ebrahim T, Pillay V, Vorster M. The Role of PET/CT in Breast Cancer. Diagnostics. Multidisciplinary Digital Publishing Institute; 2023;13:597. https://doi.org/10.3390/diagnostics13040597

3. Alberts I, Hünermund J-N, Prenosil G, Mingels C, Bohn KP, Viscione M, et al. Clinical performance of long axial field of view PET/CT: a head-to-head intraindividual comparison of the Biograph Vision Quadra with the Biograph Vision PET/CT. Eur J Nucl Med Mol Imaging. 2021;48:2395–404. https://doi.org/10.1007/s00259-021-05282-7

4. Lee JW, Lee SM. Radiomics in Oncological PET/CT: Clinical Applications. Nucl Med Mol Imaging. 2018;52:170–89. https://doi.org/10.1007/s13139-017-0500-y

5. Matheoud R, Boellaard R, Pike L, Ptacek J, Reynés-Llompart G, Soret M, et al. EFOMP's protocol quality controls in PET/CT and PET/MR. Phys Med. 2023;105:102506. https://doi.org/10.1016/j.ejmp.2022.11.010

6. Aide N, Lasnon C, Veit-Haibach P, Sera T, Sattler B, Boellaard R. EANM/EARL harmonization strategies in PET quantification: from daily practice to multicenter oncological studies. Eur J Nucl Med Mol Imaging. 2017;44:17–31. https://doi.org/10.1007/s00259-017-3740-2

7. Koole M, Armstrong I, Krizsan AK, Stromvall A, Visvikis D, Sattler B, et al. EANM guidelines for PET-CT and PET-MR routine quality control. Z Für Med Phys. 2023;33:103–13. https://doi.org/10.1016/j.zemedi.2022.08.003

8. Sagara H, Inoue K, Mano C, Kajiwara H, Nagai Y, Fujii H, et al. Usefulness of a new anthropomorphic phantom simulating the chest and abdomen regions in PET tests. Ann Nucl Med. 2025;39:303–12. https://doi.org/10.1007/s12149-024-02007-2

9. Alsyed E, Smith R, Bartley L, Marshall C, Spezi E. A heterogeneous phantom study for investigating the stability of PET images radiomic features with varying reconstruction settings. Front Nucl Med [Internet]. Frontiers; 2023 [cited 2025 Apr 27];3. https://doi.org/10.3389/fnume.2023.1078536

10. Pfaehler E, Sluis J van, Merema BBJ, Ooijen P van, Berendsen RCM, Velden FHP van, et al. Experimental Multicenter and Multivendor Evaluation of the Performance of PET Radiomic Features Using 3-Dimensionally Printed Phantom Inserts. J Nucl Med. Society of Nuclear Medicine; 2020;61:469–76. https://doi.org/10.2967/jnumed.119.229724

11. Lin H-H, Chuang K-S, Lin Y-H, Ni Y-C, Wu J, Jan M-L. Efficient simulation of voxelized phantom in GATE with embedded SimSET multiple photon history generator. Phys Med Biol. IOP Publishing; 2014;59:6231. https://doi.org/10.1088/0031-9155/59/20/6231

12. Poon JK, Dahlbom ML, Casey ME, Qi J, Cherry SR, Badawi RD. Validation of the SimSET simulation package for modeling the Siemens Biograph mCT PET scanner. Phys Med Biol. IOP Publishing; 2015;60:N35. https://doi.org/10.1088/0031-9155/60/3/N35

13. Wangerin KA, Ahn S, Wollenweber S, Ross SG, Kinahan PE, Manjeshwar RM. Evaluation of lesion detectability in positron emission tomography when using a convergent penalized likelihood image reconstruction method. J Med Imaging. SPIE; 2016;4:011002. https://doi.org/10.1117/1.JMI.4.1.011002

14. Maronnier Q, Courbon F, Caselles O. Evaluation of a method based on synthetic data inserted into raw data prior to reconstruction for the assessment of PET scanners. EJNMMI Phys. 2022;9:68. https://doi.org/10.1186/s40658-022-00496-6

15. Berthon B, Häggström I, Apte A, Beattie BJ, Kirov AS, Humm JL, et al. PETSTEP: Generation of synthetic PET lesions for fast evaluation of segmentation methods. Phys Med. 2015;31:969–80. https://doi.org/10.1016/j.ejmp.2015.07.139

16. Pfaehler E, De Jong JR, Dierckx RAJO, van Velden FHP, Boellaard R. SMART (SiMulAtion and ReconsTruction) PET: an efficient PET simulation-reconstruction tool. EJNMMI Phys. 2018;5:16. https://doi.org/10.1186/s40658-018-0215-x

17. Li S, Hamdi M, Dutta K, Fraum T, Luo J, Laforest R, et al. FAST (fast analytical simulator of tracer)-PET: an accurate and efficient PET analytical simulation tool. Phys Med Biol. 2024;69. https://doi.org/10.1088/1361-6560/ad6743

18. Castro P, Huerga C, Chamorro P, Garayoa J, Roch M, Pérez L. Caracterización y simulación de ruido en las imágenes de PET reconstruidas con OSEM: desarrollo de un método para la generación de imágenes sintéticas. Rev Esp Med Nucl E Imagen Mol. 2018;37:229–36. https://doi.org/10.1016/j.remn.2017.10.007

19. Teymurazyan A, Riauka T, Jans H-S, Robinson D. Properties of Noise in Positron Emission Tomography Images Reconstructed with Filtered-Backprojection and Row-Action Maximum Likelihood Algorithm. J Digit Imaging. 2013;26:447–56. https://doi.org/10.1007/s10278-012-9511-5

20. Rowe RW, Dai S. A pseudo-Poisson noise model for simulation of positron emission tomographic projection data. Med Phys. John Wiley & Sons, Ltd; 1992;19:1113–9. https://doi.org/10.1118/1.596774

21. Tong S, Alessio AM, Kinahan PE. Noise and signal properties in PSF-based fully 3D PET image reconstruction: an experimental evaluation. Phys Med Biol. 2010;55:1453. https://doi.org/10.1088/0031-9155/55/5/013

22. Matheson GJ, Ge L, Zhang M, Sun B, Tu Y, Zanderigo F, et al. Parametric and nonparametric Poisson regression for modeling of the arterial input function in positron emission tomography. EJNMMI Phys. 2023;10:72. https://doi.org/10.1186/s40658-023-00591-2

23. Jessen L, Gustafsson J, Ljungberg M, Curkic-Kapidzic S, Imsirovic M, Sjögreen-Gleisner K. 3D printed nonuniform anthropomorphic phantoms for quantitative SPECT. EJNMMI Phys. 2024;11:8. https://doi.org/10.1186/s40658-024-00613-7

24. Gear JI, Cummings C, Sullivan J, Cooper-Rayner N, Downs P, Murray I, et al. Radioactive 3D printing for the production of molecular imaging phantoms. Phys Med Biol. 2020;65:175019. https://doi.org/10.1088/1361-6560/aba40e

25. Gear JI, Cummings C, Craig AJ, Divoli A, Long CDC, Tapner M, et al. Abdo-Man: a 3D-printed anthropomorphic phantom for validating quantitative SIRT. EJNMMI Phys. 2016;3:17. https://doi.org/10.1186/s40658-016-0151-6

26. Nalla SKK, Maronnier Q, Hazan TP, Kennedy J, Caselles O. Enhancing PET/CT Assessment with Porous 3D Printed Grids: A Pilot Study [Internet]. medRxiv; 2025 [cited 2025 Apr 2]. p. 2025.04.01.25325022. https://doi.org/10.1101/2025.04.01.25325022

27. Gallivanone F, Interlenghi M, D'Ambrosio D, Trifirò G, Castiglioni I. Parameters Influencing PET Imaging Features: A Phantom Study with Irregular and Heterogeneous Synthetic Lesions. Contrast Media Mol Imaging. 2018;2018:5324517. https://doi.org/10.1155/2018/5324517

28. Jessen L, Curkic Kapidzic S, Gustafsson J, Larsson E, Ljungberg M, Sandström M, et al. A validation protocol for 177Lu-SPECT image quantification as a basis for multicenter kidney dosimetry. Phys Med Biol. IOP Publishing; 2025;70:115001. https://doi.org/10.1088/1361-6560/add708

29. Nalla SKK, Maronnier Q, Palchan-Hazan T, Caselles O, Kennedy J. Facilitating Multi-Center Consistency in PET/CT Assessment: Transferability and Harmonization of 3D-Printed Phantom Inserts [Internet]. medRxiv; 2025 [cited 2025 June 1]. p. 2025.05.30.25328639. https://doi.org/10.1101/2025.05.30.25328639

30. Salvador M, Kong F, Peirlinck M, Parker DW, Chubb H, Dubin AM, et al. Digital twinning of cardiac electrophysiology for congenital heart disease. J R Soc Interface. Royal Society; 2024;21:20230729. https://doi.org/10.1098/rsif.2023.0729

31. Noecker AM, Chen J-F, Zhou Q, White RD, Kopcak MW, Arruda MJ, et al. Development of Patient-Specific Three-Dimensional Pediatric Cardiac Models. Am Soc Artif Intern Organs ASAIO Platin 70th Anniv Spec Ed. CRC Press; 2024.

32. Gramigna V, Palumbo A, Fragomeni G, Gramigna V, Palumbo A, Fragomeni G. The Influence of Different ECMO Cannulation Site and Blood Perfusion Conditions on the Aortic Hemodynamics: A Computational Fluid Dynamic Model. Fluids [Internet]. Multidisciplinary Digital Publishing Institute; 2024 [cited 2025 Nov 25];9. https://www.mdpi.com/2311-5521/9/11/269. Accessed 25 Nov 2025

33. Malka-Markovitz A, Camara Dit Pinto S, Cherkaoui M, Levine SM, Anandasabapathy S, Sood GK, et al. Multiscale modeling of drug-induced liver injury from organ to lobule. Npj Digit Med. Nature Publishing Group; 2025;8:383. https://doi.org/10.1038/s41746-025-01736-6

34. Peladeau-Pigeon M, Coolens C. Computational fluid dynamics modeling of perfusion measurements in dynamic contrast-enhanced computed tomography: development, validation and clinical applications. Phys Med Biol. IOP Publishing; 2013;58:6111. https://doi.org/10.1088/0031-9155/58/17/6111

35. Peladeau-Pigeon M. Simulation of Perfusion Flow Dynamics for Contrast Enhanced Imaging. 2012 [cited 2025 June 1]; http://hdl.handle.net/1807/33495. Accessed 1 June 2025

36. Abazari MA, Soltani M, Eydi F, Rahmim A, Kashkooli FM. Mathematical modeling of 18F-Fluoromisonidazole (18F-FMISO) radiopharmaceutical transport in vascularized solid tumors. Biomed Phys Eng Express. IOP Publishing; 2024;10:065014. https://doi.org/10.1088/2057-1976/ad7592

37. Kashkooli FM, Abazari MA, Soltani M, Ghazani MA, Rahmim A. A spatiotemporal multiscale computational model for FDG PET imaging at different stages of tumor growth and angiogenesis. Sci Rep. Nature Publishing Group; 2022;12:10062. https://doi.org/10.1038/s41598-022-13345-4

38. Kreft M, Lukšič M, Zorec TM, Prebil M, Zorec R. Diffusion of d-glucose measured in the cytosol of a single astrocyte. Cell Mol Life Sci CMLS. 2012;70:1483–92. https://doi.org/10.1007/s00018-012-1219-7

39. Pan T, Einstein SA, Kappadath SC, Grogg KS, Lois Gomez C, Alessio AM, et al. Performance evaluation of the 5-Ring GE Discovery MI PET/CT system using the national electrical manufacturers association NU 2-2012 Standard. Med Phys. 2019;46:3025–33. https://doi.org/10.1002/mp.13576

40. AlMazrou RY, Alanazi SF, Alzaid MH, Al-Fakhranee RS, Ding S, Mawlawi OR. Performance characteristics of the 5-ring GE Discovery MI PET/CT scanner using AAPM TG-126 report. J Appl Clin Med Phys. 2024;25:e14315. https://doi.org/10.1002/acm2.14315

41. Sartoretti T, Skawran S, Gennari AG, Maurer A, Euler A, Treyer V, et al. Fully automated computational measurement of noise in positron emission tomography. Eur Radiol. 2024;34:1716–23. https://doi.org/10.1007/s00330-023-10056-w

42. Douglass MJJ. An open-source tool for converting 3D mesh volumes into synthetic DICOM CT images for medical physics research. Phys Eng Sci Med [Internet]. 2025 [cited 2025 July 31]; https://doi.org/10.1007/s13246-025-01599-x

Disclosures:

The MuPET framework was developed as part of a research collaboration partnership between the teams of Olivier Caselles and Sebastian Uppapalli. The authors declare that no funds, grants, or other support was received during the preparation of this manuscript. The authors declare that they have no conflicts of interest. Large language models (Gemini Pro, Curie AI) were used solely to improve the English phrasing and readability of the manuscript. All the scientific content was written and fully verified by the authors.

Abbreviations used in the article:

AAPM	American Association of Physicists in Medicine
ABS	Acrylonitrile Butadiene Styrene
AC	Activity Concentration in kBq/ml
Acq	Acquisition
ANOVA	Analysis of Variance
BPL	Bayesian penalized-likelihood reconstruction
C_i	Concentration along direction i in mol/m^3
COV	Coefficient of Variability
CTAC	Computed Tomography Attenuation Correction
CTS	Counts
D	Diffusion Coefficient
DICOM	Digital Imaging and Communications in Medicine
DMI	Discovery MI
EM	Expectation-maximization
FAST PET	Fast analytical simulator of tracer PET
FDM	Fused Deposition Modeling
FDG	Fluorodeoxyglucose
FOV	Field of View
FWHM	Full Width at Half Maximum
HU	Hounsfield Units
ISL	Inserted Synthetic Lesion
KDE	Kernel Density Estimation

K_{scale}	Noise Scale Parameter
MuPET	Multiphysics PET
MVR	Mean to Variance Ratio
n	Normal Vector
N_A	Avogadro Number
NEMA	National Electrical Manufacturing Association
PET/CT	Positron Emission Tomography/Computed Tomography
PETSTEP	PET Simulator of Tracers via Emission Projection
PSF	Point spread function
PVE	Partial volume effects
QC	Quality Control
RC	Recovery Coefficient
ROI	Region of Interest
SMART PET	SiMulAtion and ReconsTruction PET
$S_{scanner}$	Scanner sensitivity in cps/kBq
$T_{1/2}$	Half Life of Radiotracer in min
TCR	Target Contrast Ratio
TG 126	Task Group 126 Report
TOF	Time of Flight
T_{scan}	Scan Duration
VOI	Volume of Interest
V_{voxel}	Voxel Volume in mL
λ	Decay factor in s^{-1}

μ	Mean
σ	Standard Deviation
ρ	Density of radiotracer in g/mL
ϕ	Diameter